

Timing Properties of the Starlink Ku-Band Downlink

Wenkai Qin*, Andrew M. Graff†, Zachary L. Clements*, Zacharias M. Komodromos†, Todd E. Humphreys*

**Department of Aerospace Engineering and Engineering Mechanics, The University of Texas at Austin*

†*Department of Electrical and Computer Engineering, The University of Texas at Austin*

Abstract—We develop signal capture and analysis techniques for precisely extracting and characterizing the frame timing of the Starlink constellation’s Ku-band downlink transmissions. The aim of this work is to determine whether Starlink frame timing has sufficient short-term stability to support pseudorange-based opportunistic positioning, navigation, and timing (PNT). A second goal is to determine whether frame timing is disciplined to a common time scale such as GPS time. Our analysis reveals several timing characteristics not previously known that carry strong implications for PNT. On the favorable side, periods of ns-level jitter in frame arrival times across all satellite versions indicate that Starlink hardware is fundamentally capable of the short-term stability required to support GPS-like PNT. But there are several unfavorable characteristics that, if not addressed, will make GPS-like PNT impractical: (1) The v1.0 and v1.5 Starlink satellites exhibit once-per-second abrupt frame timing adjustments whose magnitude (as large as 100s of ns) and sign appear unpredictable. Similar discontinuities are also present in the v2.0-Mini frame timing, though smaller and irregularly spaced. (2) Episodic 15-s periods of high frame jitter routinely punctuate the nominal low-jitter frame arrival timing. (3) Starlink frame timing is disciplined to GPS time, but only loosely: to within a few ms by adjustments occurring every 15 s; otherwise exhibiting drift that can exceed 20 ppm. These unfavorable characteristics are essentially incompatible with accurate PNT. Fortunately, they appear to be a consequence of software design choices, not hardware limitations. Moreover, they could be compensated with third-party-provided corrections.

Index Terms—Starlink, signal characterization, positioning, time synchronization, low Earth orbit

I. INTRODUCTION

Global navigation satellite system technology (GNSS) is currently the most prevalent used for positioning, navigation, and timing (PNT). However, traditional GNSS is vulnerable to jamming and spoofing attacks that can leave users without the ability to navigate or synchronize time [1], and threats to traditional GNSS are multiplying dramatically [2]–[4]. According to OPSGROUP, an international association of air transport professionals, GNSS spoofing incidents increased by 500% from 2023 to 2024 [4]. To strengthen radionavigation, researchers have recently focused on augmenting traditional GNSS with large low Earth orbit (LEO) communications constellations [5], with some proposing a combined communications-PNT service for future constellations [6]. Because these constellations offer higher power and wider bandwidth, they are inherently resilient to adversarial interference. Further, the two-way high-rate connectivity afforded by broadband communications constellations enables desirable

features such as user authentication and near-zero age of ephemeris and clock models.

Researchers interested in a free-to-use radionavigation receiver have investigated opportunistic approaches to PNT, i.e., PNT extraction with no direct cooperation from the constellation operator and limited *a priori* knowledge regarding satellites’ ephemerides and signals. SpaceX’s Starlink constellation is of particular interest: it offers the widest signal availability, serving millions of subscribers worldwide with its 7,000+ satellites [7]. Opportunistic approaches using Starlink’s Ku-band signals (10.7–12.7 GHz) have already proven fruitful: researchers in several groups have independently demonstrated Doppler-based positioning with accuracy on the order of 10 m [8]–[14]. Unfortunately, Doppler-based techniques cannot approach the exquisite timing precision offered by traditional GNSS: even in the optimistic scenarios posed in [13], [14], timing accuracy is limited to no better than 0.1 ms. By contrast, pseudorange-based PNT from Starlink holds the potential for both meter-accurate positioning and ns-accurate timing [6], [15]. But whether Starlink signals could support precise pseudorange-based PNT remains an open question whose answer depends on the details of the broadcast signals, including modulation, timing, and spectral characteristics.

The authors of [16] uncovered key information regarding the Starlink downlink frame structure, synchronization sequences, and spectral characteristics. Follow-on work in [17] and [18] discovered other predictable elements of each frame, and [19] revealed that Starlink beam switching occurs at 15-s, approximately-GPS-aligned intervals. Other studies have shown simulated impacts of various clock types in LEO [20], or have developed methods for predicting LEO clock corrections, such as those developed for the GRACE mission [21], [22]. Nonetheless, no prior work has characterized the stability of the Starlink frame timing, nor investigated its precise relationship to an absolute time scale such as GPS time (GPST), despite these essential details being prerequisite to development of Starlink-based PNT, whether opportunistic or not.

Our paper closes this knowledge gap. We leverage the signal structure details revealed in [16] to conduct a focused study of Starlink timing properties. First, we evaluate the short-term frame clock stability, defined as the set of clock behaviors that manifest on the order of several seconds or less whose study indicates both the quality of crystal oscillator(s) onboard the Starlink satellite vehicles (SVs) and the predictability of any onboard clock corrections. Second, we investigate the absolute

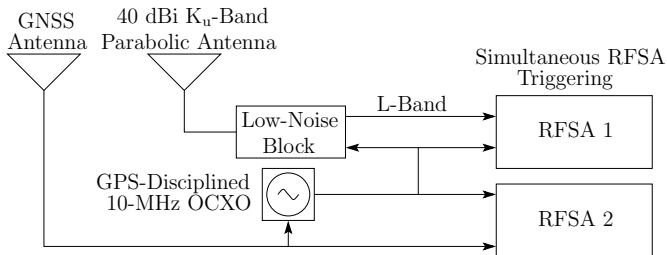


Fig. 1: Block diagram of the simultaneous Starlink and GPS signal capture system.

frame timing characteristics; i.e., we determine the extent to which Starlink frame clocks are disciplined to GPST.

A preliminary conference version of this paper appeared as [23]. The current version extends the former with a deeper examination of short-term frame clock stability, a new section analyzing absolute frame timing, a presentation of theoretical measurement bounds, and stronger conclusions.

II. SIGNAL CAPTURE

While many particulars of our signal capture system match those presented in [16], we reiterate the major signal pathways and note some updates made for the purposes of timing analysis.

Fig. 1 shows a block diagram of the signal capture system. The Starlink signal chain begins with reception of Ku-band signals through a 40 dBi parabolic dish antenna followed by frequency downconversion to L-band and signal amplification in a low-noise block (LNB). Further downconversion, amplification, filtering, and digital sampling at rates ranging from 50.0 to 62.5 Msps occur within the radio-frequency signal analyzer (RFSA) 1. This path is equivalent to the narrowband capture chain in [16].

A parallel GPS L1 capture pathway comprises an active GNSS antenna connected to an RFSA identical to RFSA 1, within which are realized the same signal processing and sampling operations as for the Starlink signal pathway. This second RFSA is denoted RFSA 2 in Fig. 1.

A key feature of the parallel capture setup is the GPS-disciplined 10-MHz oven-controlled crystal oscillator (OCXO), which drives both Starlink and GPS L1 signal pathways, allowing for synchronous capture with a unified clock model. To verify this, we captured signals from the GNSS antenna simultaneously with both RFSA, splitting the signal through equal-length cables just before insertion into each. Both data captures were then independently processed via GRID, our laboratory’s science-grade software-defined GNSS receiver [24]–[26]. By this we found that the two RFSA’s sample trains are synchronous to better than 1 ns when configured with matching sampling rates, and offset by measurable deterministic amounts when the sampling rates were not matched but were integer multiples of one another.

To measure the system’s cable delay from the Ku-band LNB to RFSA 1, required for absolute timing analysis, we performed the same experiment but routed one branch of

the split signal in a loopback configuration to near the Ku-band antenna LNB and back before insertion into RFSA 1. Dividing the observed differential latency by two yielded the unknown cable delay. Finally, to measure the additional cable delay in the GNSS capture pathway beyond that of the Starlink pathway, we substituted a GNSS antenna for the Ku-band antenna and LNB and measured the differential signal timing via simultaneous dual-RFSA capture and post-processing through GRID.

With this setup, we can capture up to 62.5 MHz of real-time Starlink bandwidth through RFSA 1 with highly stable uniform sampling, and mark each sample with a GPST timestamp to ns accuracy. This enables us to precisely determine the arrival time of a Starlink frame in GPST and study the stability of arrival times from frame to frame.

III. FRAME STRUCTURE AND SYSTEM CONCEPTS

This section introduces the Starlink frame structure, drawn from [16], and additional concepts and terminology needed to understand Starlink operation in general and Starlink-based PNT in particular.

A. Frame Structure

As shown in Fig. 2, each Starlink downlink orthogonal frequency division multiplexing (OFDM) frame consists of 302 intervals of length $T_{\text{sym}} = 4.4 \mu\text{s}$ plus a frame guard interval T_{fg} , for a total frame period of $T_f = 1/F_f$ s, where $F_f = 750$ Hz is the frame rate. Each frame begins with the primary synchronization sequence (PSS), which is natively represented in the time domain, followed by the secondary synchronization sequence (SSS), which is formatted as a standard 4QAM OFDM symbol. The final occupied symbol interval in each frame is the coda symbol (CS), which is followed by the frame guard interval. Subsequent frames may be present or not, depending on user demand.

The time-domain modulation sequence of the PSS, and the frequency-domain symbol sequence of the SSS were revealed in [16]. These sequences allow a Starlink receiver to perform the channel estimation necessary to demodulate each OFDM symbol in the frame. In particular, the PSS allows the receiver to precisely identify the beginning of each frame, while the SSS allows it to perform equalization across all subcarriers. The PSS and SSS have a fixed phase relationship, which allows coherent integration across the combined PSS + SSS interval, permitting more accurate synchronization and carrier frequency offset (CFO) estimation, as will be further examined in Section V.

The role of the CS, called the CSS in [16], is not entirely clear. Its frequency-domain symbol sequence is highly predictable, but not entirely so, unlike the SSS [17]. Likewise, other OFDM symbols in each frame have varying degrees of predictability, whether due to pilot symbols meant to aid channel estimation or to default symbols transmitted when user data do not occupy all the payload-bearing symbols in a frame [17], [18]. For the timing analysis in this paper, the local signal replica used for correlation comprises only the coherent PSS + SSS combination so that, insofar as possible, results are uniform across all received frames.

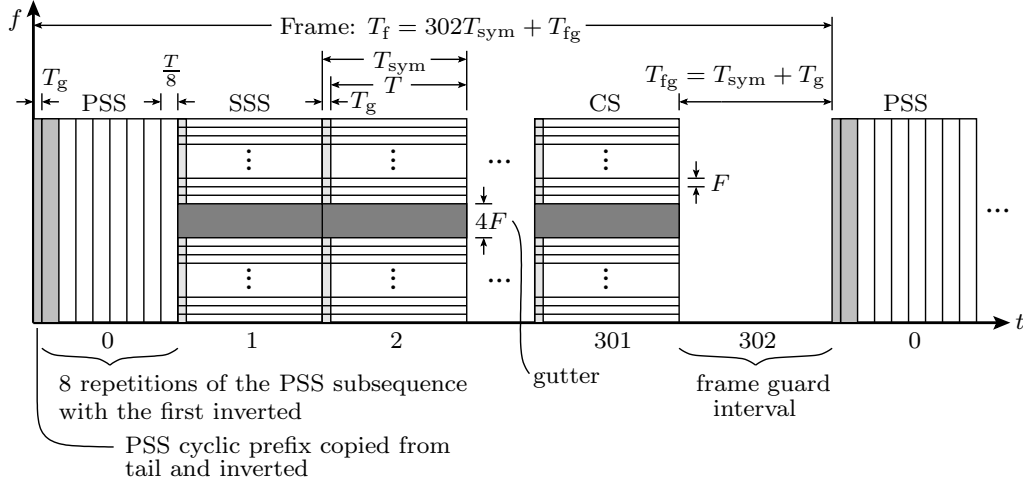


Fig. 2: Frame layout for the Ku-band Starlink downlink along time-frequency dimensions, from [16]. Indices along the horizontal axis enumerate the 303 intervals that constitute a single frame. The quantity T is the useful (non-cyclic) OFDM symbol interval, T_g is the symbol guard interval (cyclic prefix), and F is the subcarrier spacing. Other quantities are defined in the text.

B. Assigned Beams

At any given time, a user within Starlink's $\pm 53^\circ$ latitude primary coverage area may have a direct line of sight to dozens of overhead SVs above 20° elevation [6]. Each Starlink SV is capable of simultaneously directing up to 48 downlink beams to terrestrial service cells, 16 for each of its three downlink phased arrays. A proprietary beam assignment procedure assigns each beam to a ~ 20 -km-diameter service cell [27]. A service cell may be illuminated by up to 16 beams simultaneously, two beams for each of the eight frequency channels identified in [16]. We call the N_{bi} beams deliberately directed to the i th service cell *assigned beams*.

The number of distinct SVs casting assigned beams onto the i th service cell, $N_{asi} \leq N_{bi} \leq 16$, may be less than N_{bi} because a given SV may project multiple beams onto the same cell, each on a different channel or with a different polarization (right-hand vs. left-hand circular polarization). As Starlink user density has increased over the past few years, N_{asi} and N_{bi} have generally increased. It was shown in [19] that a search procedure prioritizing high-elevation SVs was effective at finding multiple illuminating SVs.

C. Fixed Assignment Interval

Several publications have noted the existence of a 15-s Starlink network reconfiguration interval [19], [28]–[30]. Because all beam assignments remain fixed over the duration of this interval, we call it the *fixed assignment interval* (FAI). FAI boundaries appear to be approximately aligned with GPST [19]. As discussed later, noticeable transitions in Starlink frame timing behavior occur at FAI boundaries. Accordingly, we split captures along FAI boundaries when analyzing frame clock behaviors.

We write $N_{bi}(l)$ to indicate the number of assigned beams for the i th cell during the l th FAI, and $N_{asi}(l) \leq N_{bi}(l) \leq 16$ to indicate the number of distinct SVs casting assigned beams onto the i th cell during the l th FAI.

D. Side Beams

Assigned beams are not the only ones from which a receiver in a given service cell may extract PNT information. Consider Fig. 3, which shows the normalized cross-correlation of a short interval of received Starlink data against a local signal replica composed of a coherent PSS + SSS combination. The highest correlation peaks shown correspond to frames from an assigned beam, whereas the weaker peaks correspond to frames from *side beams*, or beams directed toward other service cells. The assigned beam's pre-correlation SNR over this interval is approximately 21 dB, whereas for the side beam corresponding to the lower circled correlation peaks the pre-correlation SNR is only 3 dB. Despite their lower SNR, it is possible to extract time of arrival (TOA) measurements from such side-beam peaks precisely enough to support GPS-like PNT.

The post-correlation SNR of side-beam correlation peaks depends on the side beam's pre-correlation SNR and on the processing gain afforded by correlation against known synchronization sequences or other predictable elements of a frame. Reference [31] shows that correlation against a coherent PSS + SSS replica can support reliable signal detection across a large blind Doppler and time offset search space at a low false alarm rate provided that frames have a pre-correlation SNR higher than -18 dB. If the receiver can somehow assemble a local replica of an entire frame, whether because a Starlink SV transmits a known default frame during a time of low user demand [17], or because a third party receives the frame through a high-gain antenna and provides its contents through a side channel to the receiver, the full-frame processing gain makes it possible to reduce the detection threshold for pre-correlation SNR to -40 dB [31]. A later section will examine frame TOA measurement precision as a function of pre-correlation SNR and processing gain. For now, suffice it to say that useful TOA measurements could be extracted from all the minor peaks visible in Fig. 3.

There are two possible scenarios under which side beams

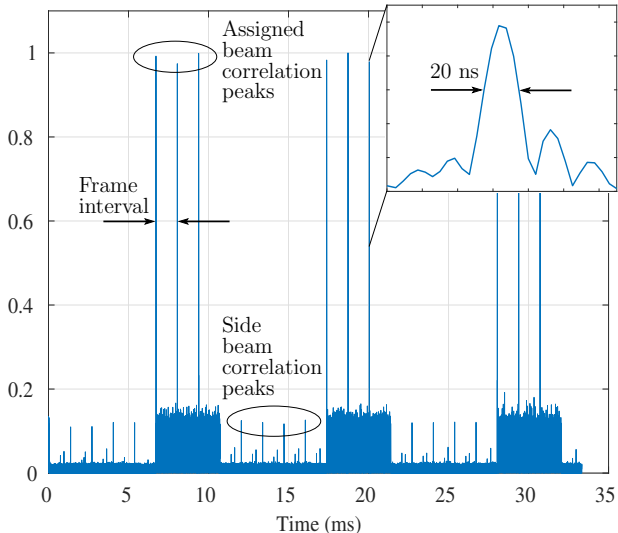


Fig. 3: Normalized cross-correlation of received Starlink data against a local PSS + SSS replica yields sharp peaks at the beginning of each frame. The peaks’ primary lobe is approximately 20 ns wide for a 55-MHz-bandwidth capture. The nominal interval between frames is $T_f = 1/750$ s. The data shown are for STARLINK-30580, a v2.0-Mini SV, from signals captured in February 2024, but the frame correlation pattern is broadly representative of signals captured since 2022 for v1.0, v1.5, and v2.0-Mini SVs.

may be observed. First, the side lobes of a beam may be strong enough for the beam to be detectable by a receiver in a service cell different from the one to which the beam is assigned. Signals received in this way may be severely attenuated: for the Ku-band communications SVs studied in [32], the downlink phased array’s side lobes were attenuated by ~ 30 dB relative to the main lobe.

Second, spillover from a beam assigned to a cell near the one occupied by the receiver can yield a detectable side beam. A beam’s main lobe creates a ground coverage region whose shape can be modeled as the elliptical intersection of a cone aligned with the main lobe’s boresight and Earth’s surface [33]. Let R_{bi} represent, for a given processing gain and for a beam assigned to the i th service cell, the region within which a receiver may reliably extract precise TOA measurements, and let R_{ci} be the i th hexagonal Starlink service cell. For reliable broadband service, it must be the case that $R_{ci} \subset R_{bi}$. Moreover, recognizing that the SNR requirement for TOA measurement is much lower than that for broadband communications, one expects the spillover region $R_{soi} \triangleq R_{bi} \setminus R_{ci}$ to be large. This is especially so given that R_{bi} ’s elliptical eccentricity varies inversely with the assigned beam’s elevation angle viewed from its target service cell [33], and given that Starlink seeks to lower its minimum transmission elevation angle from 25° to 20° [34]. Thus, spillover-induced side beams are expected to be plentiful.

We denote by $N_{si}(l) \geq N_{asi}(l)$ the total number of SVs from which a receiver in the i th service cell may reliably extract precise TOA measurements during the l th FAI. Due to the

presence of side beams, $N_{si}(l)$ may be significantly larger than $N_{asi}(l)$. For Starlink-based PNT, larger $N_{si}(l)$ ensures solution robustness and tends to increase the geometric diversity of a navigation solution, which decreases the solution’s dilution of precision [35].

E. Signal Terminology

Captured signals may include simultaneous transmissions from both assigned and side beams. We define a *composite signal* as one with significant power contributions from multiple beams, whereas a *simplex signal* contains significant power only from a single beam. Within a composite signal capture, the strongest transmission from a single beam is referred to as the *dominant signal*, while weaker transmissions from other beams are called *secondary signals*. Typically, the dominant signal corresponds to an assigned beam.

We identify a particular sequence of correlation peaks during a given FAI as corresponding to a unique beam by a two-factor test: (1) the peaks have approximately the same magnitude, and (2) the peaks are spaced from one another by integer multiples of $T_f = 1/F_f = 1/750$ s according to the relevant frame clock. Given a sufficiently long capture within a single FAI, this test is adequate to associate all correlation sequences of significant magnitude with their respective beams. Thus, for example, the largest 9 peaks in Fig. 3 correspond to frames from a unique assigned beam, and the set of 12 lower peaks, including the four lower circled ones, correspond to frames from a unique side beam.

To classify single-beam signals as dominant or secondary, we estimate their SNR by comparing post-correlation peaks with a noise floor estimate, derived from the complex signal variance in intervals presumed to lack active transmissions. However, strictly speaking, it is not always possible to ensure the noise floor estimate is completely free of secondary signals.

Whether a given captured signal is composite or simplex depends on the processing gain afforded by the local signal replica. For a coherent PSS + SSS replica, as in Fig. 3, signals with pre-correlation SNR below -18 dB are effectively undetectable [31], rendering them insignificant as secondary signals.

IV. CLOCK MODELS

As with any analysis of PNT systems based on radio wave propagation, unambiguous models of the various clocks involved are key to understanding and characterizing the system.

A. Beam-Specific Clock Cascade Model

Fig. 4 presents a clock cascade model for a single Starlink downlink beam. The model is beam-specific because, as will be shown later on, frame timing behavior may differ from beam to beam over the same FAI for the same SV. This remarkable observation implies that Starlink signal timing is much different from that of traditional GNSS, in which a single clock governs the whole transmission cascade across all frequencies. To be sure, in traditional GNSS timing offsets

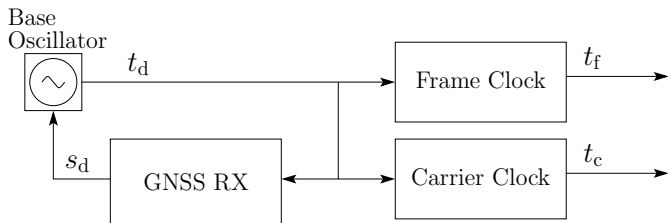


Fig. 4: Clock cascade model for a single Starlink downlink beam.

may be present between different spreading codes on the same carrier and across multiple carriers, resulting in so-called differential code biases [36]. But the code rates as transmitted are all a constant multiple of a single base clock’s reference frequency. By contrast, the frame sequences on different beams from the same Starlink SV may differ in both time offset and rate, a fact with significant implications for Starlink-based PNT.

The root of each clock cascade is a base oscillator. As will be shown, this oscillator is shared across all beams from a given SV. An onboard GNSS receiver driven by the base oscillator produces a clock disciplining signal s_d that corrects the base oscillator towards GPST. Together, the base oscillator and the GNSS receiver form a closed feedback loop that produces the GNSS-disciplined timing signal t_d .

B. Frame and Carrier Clocks

The GNSS-disciplined timing signal t_d drives the frame and carrier clocks. In turn, the frame clock’s signal t_f governs the timing of frames transmitted by the SV, and the carrier clock’s signal t_c drives the carrier onto which the information-bearing frames are modulated. The frame clock is likely a software-based clock whose output t_f depends on when baseband frames are loaded into buffers for mixing to radio frequency (RF) and subsequent transmission. The carrier clock is likely transparent, meaning that $t_c = t_d$, but it is represented in a manner identical to the frame clock for full model generality.

Note that in traditional GNSS the clock driving each SV’s spreading code (analogous to the frame clock) also drives the underlying carrier that the spreading code modulates [37]. Thus, the code and the carrier—as transmitted—are locked together such that the code chipping rate is a constant rational multiple of the carrier frequency. One of this paper’s key findings, elaborated later, is that such is not the case for the Starlink Ku-band downlink signals. Instead, the frame and carrier clocks operate somewhat independently, which is why they are represented separately in Fig. 4.

We represent frame and carrier clock offsets from t_d as Δt_f and Δt_c . These are related to t_d , t_f , and t_c by

$$t_d(t) = t_f(t) - \Delta t_f(t) \quad (1)$$

$$t_d(t) = t_c(t) - \Delta t_c(t) \quad (2)$$

where t represents true time, or time according to an ideal clock, such as is closely realized by GPST [38]. In this paper,

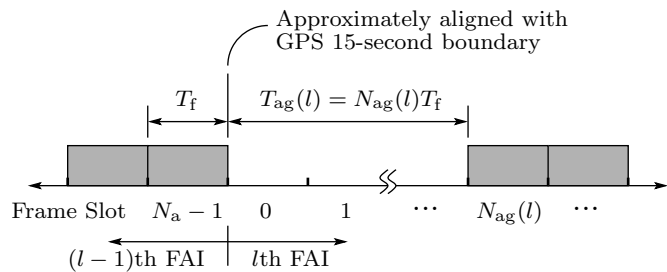


Fig. 5: Frame sequence timing diagram showing the transition from the $(l - 1)$ th FAI to the l th FAI.

true time and GPST are taken to be synonymous. The frame and carrier clocks are related to t by

$$t = t_f(t) - \delta t_f(t) \quad (3)$$

$$t = t_c(t) - \delta t_c(t) \quad (4)$$

where $\delta t_f(t)$ and $\delta t_c(t)$ are the frame and carrier clock offsets.

The time derivatives of $\delta t_f(t)$ and of $\delta t_c(t)$ are called the frame and carrier clock drift. They are equivalent to the instantaneous fractional frequency deviation, written generically as $y(t)$, on which clock stability analysis is based [39].

C. Discrete-Time Frame Clock

The frame sequence timing diagram in Fig. 5 offers further details about the frame clock. Each frame as transmitted has a duration of exactly T_f according to the frame clock. Within each FAI, the frame slot index increments from 0 to $N_a - 1$, with $N_a = 11250$ being the number of frame slots in one FAI. Each FAI starts at the beginning of frame slot 0 and lasts $N_a T_f = 15$ s. The interval of unoccupied frame slots at the beginning of the l th FAI, called the FAI guard interval $T_{ag}(l) = N_{ag}(l)T_f$, spans a variable number of frame slots $N_{ag}(l)$. Note that, for any FAI index l , frame slot $N_{ag}(l)$ is occupied by definition, but other frame slots may not be occupied.

Let $t_f(l, m)$ be the frame clock time at the instant when the frame in the m th frame slot of the l th FAI begins to pass through the phase center of the SV’s downlink antenna, where l and m are zero-based indices. By definition, we take this to be

$$t_f(l, m) \triangleq 15l + mT_f \quad (5)$$

Let $t^*(l, m)$ and $\delta t_f(l, m)$ be the corresponding GPST and frame clock offset. Then

$$t^*(l, m) = t_f(l, m) - \delta t_f(l, m) \quad (6)$$

Another of this paper’s key findings is that $\delta t_f(l, 0) \approx 0$. Stated differently, a Starlink SV’s frame clock departure from GPST at the beginning of each FAI is small—typically less than a few ms.

D. Receiver Clock

Now consider the clock of a receiver tracking signals from the Starlink downlink. The receiver clock time t_r is related to true time t by

$$t = t_r(t) - \delta t_r(t_r) \quad (7)$$

The receiver clock offset $\delta t_r(t_r)$ is represented as a function of t_r because it is natively ordered in receiver time in the course of solving for a position and time solution. The time derivative of δt_r with respect to t , denoted $\delta \dot{t}_r(t_r(t))$, is called the receiver clock drift.

Let $t_r(l, m)$ be the time of reception, according to the receiver clock, of the frame transmitted at true time $t^*(l, m)$. Let $\delta t_r(l, m)$ be the corresponding receiver clock offset and $t_*(l, m)$ be the corresponding true time of reception. More precisely, $t_r(l, m)$ is the receiver clock time at which the frame transmitted at true time $t^*(l, m)$ from the satellite's downlink antenna's phase center first reached the receiver antenna's phase center. The receipt time $t_r(l, m)$ can be related to $t_*(l, m)$, $t^*(l, m)$, and $t_f(l, m)$ by

$$t_*(l, m) = t_r(l, m) - \delta t_r(l, m) \quad (8)$$

$$t^*(l, m) = t_r(l, m) - \delta t_r(l, m) - \delta t_{\text{tof}}(l, m) \quad (9)$$

$$t_f(l, m) = t_r(l, m) - \delta t_r(l, m) - \delta t_{\text{tof}}(l, m) + \delta t_f(l, m) \quad (10)$$

where $\delta t_{\text{tof}}(l, m)$ is the frame's time of flight from transmission to reception, expressed as an interval in true time.

V. MEASUREMENT ERROR BOUNDS

Here we provide theoretical bounds on the Doppler and TOA error variance based on channel estimation using the PSS + SSS. We do this both to illustrate the level of precision possible with Starlink-based PNT and to prepare for later analysis investigating the relationship between frame and carrier Doppler.

A. Doppler Error Variance

A lower bound on Doppler frequency error variance for a signal $s(t)$ with energy E , noise spectral density N_0 , and mean time epoch t_0 can be expressed in the form [40, Eq. 11.27]

$$\sigma_{f_b}^2 \geq \frac{1}{2\alpha^2 \frac{E}{N_0}} \quad (11)$$

where α^2 is the effective squared time duration, defined as

$$\alpha^2 \triangleq \frac{\int_{-\infty}^{\infty} (2\pi(t - t_0))^2 |s(t)|^2 dt}{\int_{-\infty}^{\infty} |s(t)|^2 dt} \quad (12)$$

The PSS signal given in [16, Eq. 34] has an effective time duration of $\alpha_{\text{PSS}} = 7.745 \mu\text{s}$, while the SSS signal given in [16, Eq. 37] has an effective time duration of $\alpha_{\text{SSS}} = 7.8428 \mu\text{s}$. The coherent combination of PSS and SSS in a single frame results in $\alpha_1 = 15.975 \mu\text{s}$, and the coherent combination across two frames results in $\alpha_2 = 4.2 \text{ms}$.

Fig. 6 plots the Doppler frequency root-mean-square error (RMSE) bound in units of Hz for the PSS-only, SSS-only, single-frame PSS + SSS, and two-frame PSS + SSS signals (i.e., coherent correlation across the PSS + SSS combination in a pair of adjacent frames). One may conclude from Fig. 6 that a Doppler estimation based on a single coherent PSS + SSS interval yields an RMSE far worse than assumed in [13]. Clearly, for Doppler-based Starlink PNT, coherent processing across many more than two OFDM symbols will be required.

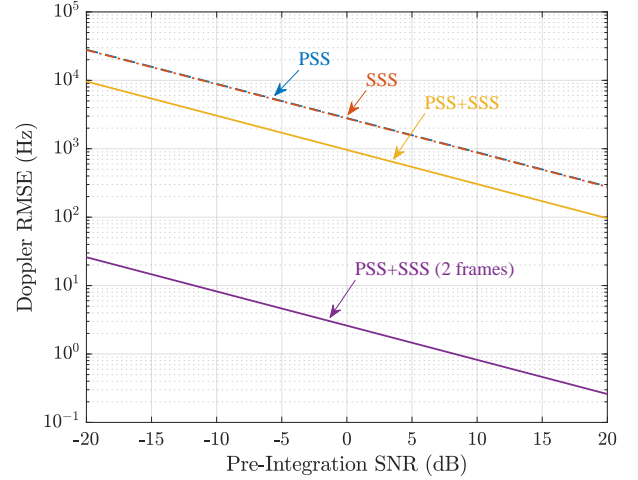


Fig. 6: Doppler frequency RMSE bounds for various combinations of coherent processing based on the PSS and SSS.

B. Time of Arrival Measurement Error Variance

Similar to the foregoing Doppler frequency bound, a lower bound on TOA error variance for a signal with Fourier transform $S(f)$, energy E , and noise spectral density N_0 can be expressed in the form [40, Eq. 11.15]

$$\sigma_\tau^2 \geq \frac{1}{2\gamma^2 \frac{E}{N_0}} \quad (13)$$

where γ^2 is the effective squared bandwidth defined as

$$\gamma^2 \triangleq \frac{\int_{-\infty}^{\infty} (2\pi f)^2 |S(f)|^2 df}{\int_{-\infty}^{\infty} |S(f)|^2 df}. \quad (14)$$

The PSS signal given in [16, Eq. 34] has a Fourier transform

$$S_{\text{PSS}}(f) \triangleq \frac{1}{F_s} \sum_{k=-N_g}^{N-1} \text{rect}\left(\frac{f}{F_s}\right) \exp\left(-j2\pi(k + N_g)\frac{f}{F_s}\right) p_k \quad (15)$$

and an effective bandwidth of $\gamma_{\text{PSS}} = 4.3482 \times 10^8 \text{ Hz}$. Similarly, the SSS signal given in [16, Eq. 1.37] has a Fourier transform

$$S_{\text{SSS}}(f) \triangleq \sum_{k=-\frac{N}{2}}^{\frac{N}{2}-1} X_{m1k} \exp(-j2\pi F T_g k) G_s(f - Fk) \quad (16)$$

$$G_s(f) \triangleq \mathcal{F}[g_s(t)] = T_{\text{sym}} \text{sinc}(T_{\text{sym}} f) \exp(-j\pi T_{\text{sym}} f) \quad (17)$$

and an effective bandwidth of $\gamma_{\text{SSS}} = 4.3658 \times 10^8 \text{ Hz}$. The PSS and SSS signal combined in a single frame have a Fourier transform of $S_1(f) = S_{\text{PSS}}(f) + \exp(-j2\pi T_{\text{sym}} f) S_{\text{SSS}}(f)$. In the case of coherent processing of the PSS + SSS across two frames, this becomes $S_2(f) = S_1(f) + \exp(-j2\pi T_f f) S_1(f)$.

Fig. 7 plots the TOA RMSE bound in units of meters for the PSS-only, SSS-only, single-frame PSS + SSS, and two-frame PSS + SSS signals. Due to the large bandwidth of the synchronization sequences, sub-centimeter accuracy is theoretically achievable at moderate SNR.

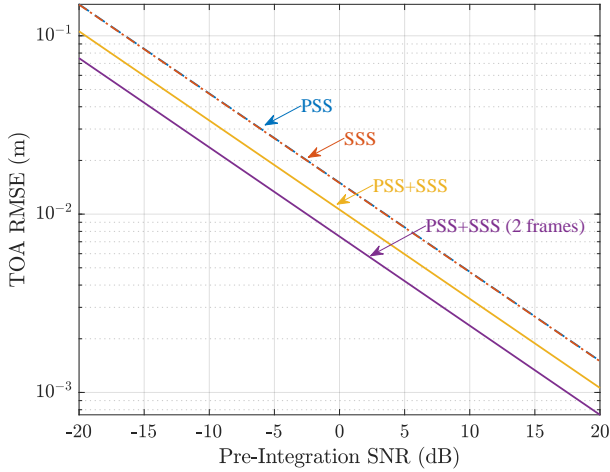


Fig. 7: TOA RMSE bounds for various combinations of coherent processing based on the PSS and SSS.

VI. DATA PREPROCESSING

We capture Starlink signals through RFSA 1 as shown in Fig. 1 at a complex sampling rate ranging from 50.0 to 62.5 MHz. Captured signals are then upsampled to the Starlink information symbol rate $F_s = 240$ MHz so that all subsequent operations may proceed as if the full 240-MHz Starlink channel bandwidth had been captured. The upsampled signal is cross-correlated against a local signal replica consisting of the coherent PSS + SSS combination to produce correlation peaks like those shown in Fig. 3. For the m th frame, let

$$x_{m01}(t) \triangleq \begin{cases} x_{m0}(t), & 0 \leq t < T_{\text{sym}} \\ x_{m1}(t - T_{\text{sym}}), & T_{\text{sym}} \leq t < 2T_{\text{sym}} \\ 0, & \text{otherwise} \end{cases} \quad (18)$$

be the coherent concatenation of the time-domain PSS and SSS functions from [16]. Because the PSS and SSS are present in all Starlink downlink frames and are identical for all frames $m \in \mathbb{Z}$ and all SVs, $x_{m01}(t)$ can be used for correlation against all captured data.

The full discrete-time local signal replica used for correlation is the product of $x_{m01}(t)$ and a complex exponential:

$$y_{m01}[k] \triangleq x_{m01}(kT_s(1 - \beta)) \exp(j2\pi [F_c(1 - \beta) - \bar{F}_c] kT_s) \quad (19)$$

Here, $T_s = 1/F_s$ is the sampling interval, F_c is the center frequency of the OFDM channel, β is the CFO parameter, and $\bar{F}_c \approx F_c$ is the center frequency to which the receiver is tuned. Correlation proceeds in blocks of between 30 and 60 frame intervals T_f . Over each block, a constant β is applied that maximizes correlation peak magnitudes within the block. This process amounts to batch sequential frequency tracking.

A high-precision TOA measurement is extracted from the correlation peak for each frame received. Unless otherwise noted, all frame timing measurements were extracted from dominant signals with pre-correlation SNR exceeding -1 dB, which, upon correlation against the replica signal in (19), yields a post-correlation SNR of at least 25 dB for a ≥ 50 -MHz captured bandwidth [31]. Let \mathcal{M}_l be the set of occupied-

frame indices for the l th FAI. A sequence of frame TOA measurements corresponding to \mathcal{M}_l is extracted from the cross-correlation function. These are modeled as

$$\tilde{t}_r(l, m) = t_r(l, m) + w_r(l, m), \quad m \in \mathcal{M}_l \quad (20)$$

where $w_r(l, m)$ is zero-mean Gaussian measurement error with variance $\sigma_w^2(l, m)$. The m th measurement $\tilde{t}_r(l, m)$ is the receiver time of the discrete sample instant at which the correlation peak for the m th frame is maximized. As can be appreciated by examining the zoomed inset in Fig. 3, the measurement errors $\{w_r(l, m) \mid m \in \mathcal{M}_l\}$ contain errors due to (1) nearest-sample quantization of the maximizing location, (2) thermal noise, and (3) peak rounding caused by filtering in the RFSA for the relatively narrow bandwidth captured (e.g., 55 MHz for Fig. 3 as compared to the full $F_s = 240$ -MHz bandwidth). Their empirical standard deviation is approximately $\sigma_w = 2$ ns, or 0.6 m in equivalent length, which is well above the single-frame PSS + SSS RMSE bound for $\text{SNR} \geq -1$ in Fig. 7. Nonetheless, this level of measurement precision is more than adequate to study the short- and long-term Starlink frame clock behavior because, as will be shown, variations in $\delta t_f(t)$ are typically much larger than 2 ns.

VII. SHORT-TERM FRAME CLOCK STABILITY

This section explores short term (within a single FAI) Starlink frame clock behavior. The emphasis here is on relative timing and high-frequency variations in the frame clock offset δt_f , as opposed to absolute timing and low-frequency variations. Rearranging (10) to isolate $\delta t_f(l, m)$ yields

$$\delta t_f(l, m) = t_f(l, m) - t_r(l, m) + \delta t_r(l, m) + \delta t_{\text{tof}}(l, m) \quad (21)$$

Let $\delta t'_f(l, m)$ be equivalent to $\delta t_f(l, m)$ but with a 3rd-order polynomial fit across all $m \in \mathcal{M}_l$ removed. Assume like notation for the other terms in (21). Analysis of $\delta t'_f(l, m)$ is sufficient to characterize the short-term properties of the frame clock because $\delta t'_f(l, m)$ retains the high-frequency variations present in $\delta t_f(l, m)$. The detrended $\delta t_f(l, m)$ can be modeled as

$$\begin{aligned} \delta t'_f(l, m) &= t'_f(l, m) - t'_r(l, m) + \delta t'_r(l, m) + \delta t'_{\text{tof}}(l, m) \\ &\approx -t'_r(l, m) \\ &\approx -\tilde{t}'_r(l, m) \end{aligned} \quad (22)$$

This approximation is explained as follows: For $m \in \mathcal{M}_l$, $t_f(l, m)$ is an affine function of m , which implies $t'_f(l, m) = 0$. Likewise, $\delta t'_r(l, m) \approx 0$ because the receiver clock is a GPS-disciplined OCXO with negligible frequency error. Finally, $\delta t'_{\text{tof}}(l, m) \approx 0$ because the time of flight to an SV in LEO can be modeled to better than 1 ns over a 15-s FAI as a 3rd-order function.

In summary, for purposes of a short-term frame clock stability analysis, $\delta t'_f(l, m)$ is a valid proxy for $\delta t_f(l, m)$, and $\tilde{t}'_r(l, m)$, the 3rd-order-polynomial-detrended version of the frame TOA measurement $\tilde{t}_r(l, m)$, is equivalent to $\delta t'_f(l, m)$ to within a sign reversal and the ns-level measurement error $w_r(l, m)$.

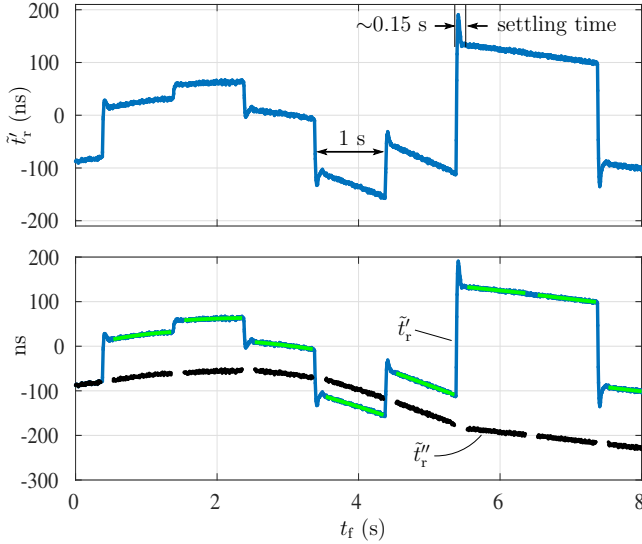


Fig. 8: Top: \tilde{t}'_r vs. t_f for an example capture occurring within a single FAI. Bottom: \tilde{t}'_r (blue), piecewise 2nd-order polynomial fits to the truncated inter-adjustment segments (green), and \tilde{t}''_r , truncated inter-adjustment segments with first-order discontinuity eliminated (black). The data shown are for STARLINK-5141, a v1.5 SV, from signals captured in November 2023.

Note that until near the end of this section, we limit our analysis to v1.0 and v1.5 SVs, as their frame clocks behave differently from those of v2.0-Mini SVs.

A. Periodic Frame Clock Adjustments

The top panel of Fig. 8 shows an example \tilde{t}'_r trace for an 8-s interval within a single FAI. Interpreting \tilde{t}'_r as a proxy for the detrended frame clock deviation $\delta t'_f$, it is clear that the Starlink frame clock exhibits abrupt adjustments at a regular 1-Hz cadence. We believe these are the result of coarse GNSS disciplining of the base oscillator. Similar adjustments at the same 1-Hz cadence were evident in every capture of signals from Starlink v1.0 and v1.5 SVs. If due to GNSS disciplining, such large and frequent adjustments—up to several hundred ns at 1 Hz—reflect a base oscillator with poor stability.

Abrupt and coarse adjustments to the frame clock are obviously undesirable for pseudorange-based PNT. Unless they can be modeled or eliminated by some differential scheme, such adjustments would cause large errors in pseudorange modeling, and thus in position and timing estimation. They act, in effect, like the clock dithering implemented to intentionally degrade GPS accuracy under the Selective Availability program discontinued in May 2000 [41].

To assess their predictability and other characteristics, we analyzed 281 adjustments associated with 12 unique Starlink v1.0 and v1.5 SVs and made the following observations.

1) *Cadence*: Frame clock adjustment opportunities occur at an almost perfectly regular 1-Hz cadence. Of the 281 adjustments studied, all but one arrived within a few ms of an integer second from the previous one, according to the frame clock t_f . The single outlier, from a STARLINK-5666 (v1.5) capture, arrived 100 ms earlier than expected. At each

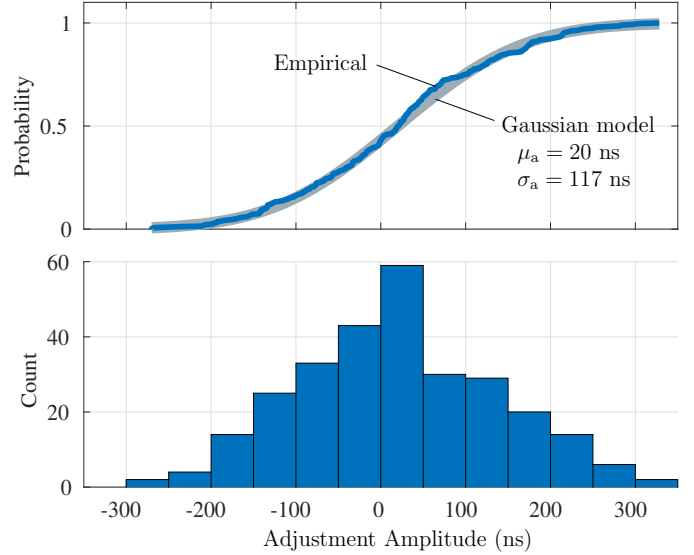


Fig. 9: Top: Cumulative probability distribution for Starlink v1.0 and v1.5 frame clock adjustment amplitudes. Bottom: Histogram of adjustment amplitudes.

opportunity, an adjustment may occur or not—note the lack of adjustment at 6.5 s in Fig. 8.

2) *Alignment with Respect to FAI*: One might expect frame clock adjustment opportunities to be aligned to the FAI such that 15 inter-adjustment intervals fit neatly within one FAI. This is not the case; there appears to be no fixed relationship between FAI boundaries and the 1-Hz adjustment opportunities. On this observation and a supporting one presented in Section IX rests our decision to model the GNSS disciplining of the base oscillator as occurring prior to and independent of any further adjustments made by the frame clock, as illustrated in Fig. 4. Thus, the frame clock t_f exhibits the 1-Hz disciplining adjustments present in t_d , but the adjustment amplitude and timing are not coordinated with the frame timing.

3) *Probability Distribution of Adjustment Amplitudes*: If the 1-Hz frame clock adjustments were quantized (say, occurring only in 20-ns steps), this would offer hope of developing an adjustment compensation mechanism within a pseudorange-based position and time estimator. Alas, this is not the case. Instead, the adjustment amplitudes appear to be smoothly distributed with mean $\mu_a = 20$ ns and standard deviation $\sigma_a = 117$ ns, as shown in Fig. 9. A Shapiro-Wilk goodness-of-fit test for normality yielded $p = 0.3$, suggesting a reasonably close alignment with the Gaussian distribution [42].

With $\sigma_a = 117$ ns, the adjustment amplitudes are commensurate with the symbol guard interval (the cyclic prefix) for Starlink’s OFDM symbols, which is $T_g = 133$ ns [16]. Thus, one might expect the adjustments to cause inter-symbol interference (ISI) and thus a degradation in communications throughput. But close inspection reveals that the adjustments are not instantaneous: they occur slowly relative to the OFDM symbol rate, with a rise time of about 25 ms and a settling time of 150 ms. Thus they pose no risk of increased ISI.

4) *Frequency Adjustments*: For further insight into adjustment characteristics, we smooth \tilde{t}_r' by eliminating the time shifts due to the 1-Hz adjustments. To perform this smoothing, we fit a 2nd-order polynomial to the inter-adjustment segments in \tilde{t}_r' , truncated to exclude the leading 0.15 s and final 0.02 s of data to avoid the adjustments' transient effects. The truncated inter-adjustment polynomial fits are shown in green in the bottom panel of Fig. 8. They and their corresponding data segments are then shifted in such a way as to minimize first-order discontinuity. That is, for each inter-adjustment segment in the FAI, we minimize the difference between the final value of the segment's shifted polynomial fit and the initial value of the next segment's shifted fit.

The resulting time series, denoted \tilde{t}_r'' and exemplified by the black trace in the bottom panel of Fig. 8, reveals that the 1-Hz disciplining adjustments not only impose a time shift in the base oscillator's time t_d but also a frequency shift. Note in Fig. 8 the abrupt change in the slope of \tilde{t}_r'' at the adjustment opportunity just prior to $t_f = 6$ s. As with time shifts, frequency shifts were found to occur randomly at each adjustment opportunity and exhibit apparently random, unquantized amplitudes. The presence of frequency adjustments further complicates any effort at modeling δt_f to obtain accurate position and time estimates from pseudorange measurements.

B. Nominal Jitter

A further processing step allows us to assess the high frequency variations (jitter) in \tilde{t}_r . We subtract from \tilde{t}_r' the 2nd-order polynomial fits (the green segments in Fig. 8) of each truncated inter-adjustment segment to flatten the time series. We denote this flattened time series as \tilde{t}_r''' , an example of which is shown in the top plot of Fig. 10. Under nominal conditions for v1.0 and v1.5 SVs, the RMS value of \tilde{t}_r''' ranges between 1.7 and 2.5 ns. A large contributor to this jitter is nearest-sample quantization noise, which, for $y_{m01}[k]$ from (19) sampled at $F_s = 240$ MHz, has an RMS value of $1/\sqrt{12}F_s = 1.2$ ns [43]. Assuming this noise is independent of other sources of jitter, the RMS contribution of the other sources ranges from 1.5 to 2.2 ns. Some of this is due to thermal noise in the receiver, so 2.2 ns serves as an upper bound on the jitter in the SVs' frame clock deviation δt_f under nominal behavior. This implies that the frame clock of Starlink v1.0 and v1.5 SVs is capable of maintaining jitter at the ns level, which, setting aside the 1-Hz time and frequency adjustments and the lower-frequency variations in δt_f , is adequately low to support accurate pseudorange-based PNT.

C. Short-Term Frame Clock Stability Bound

To probe the stability limits of the v1.0 and v1.5 Starlink SV frame clocks, we performed an Allan deviation analysis of \tilde{t}_r''' time histories, such as the black trace in Fig. 8, for 18 separate FAIs. The duration of these \tilde{t}_r''' time histories ranged from 10 to 15 s. The data originate from 9 unique v1.0 and v1.5 Starlink SVs whose signals were captured during 2022 and 2023 and whose frame timing was derived from

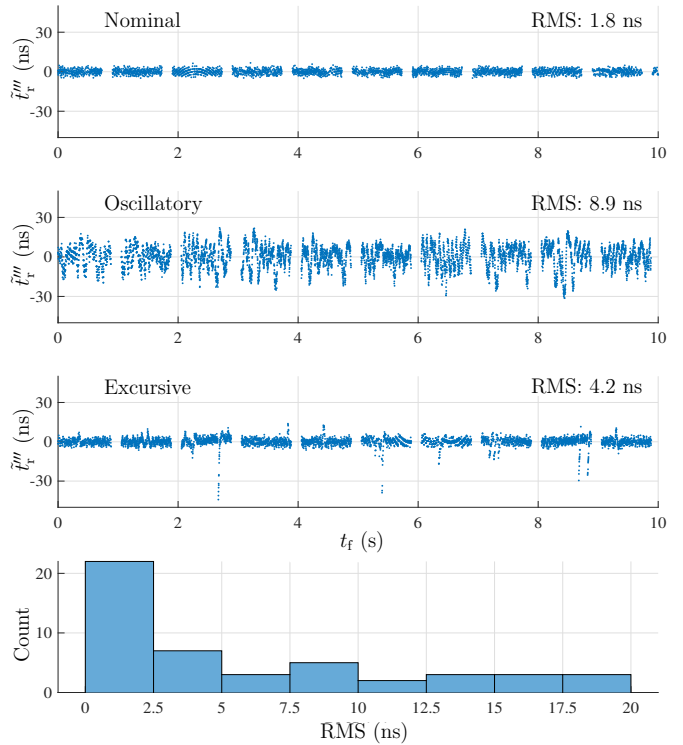


Fig. 10: Top three panels: The flattened time series \tilde{t}_r''' for the same Starlink SV during three contiguous FAIs, showing nominal, oscillatory, and excursive high-frequency frame clock behavior. The data shown are for STARLINK-2119, a v1.0 SV, from signals captured in November 2023. Bottom panel: Histogram of per-FAI \tilde{t}_r''' RMS values for all v1.0 and v1.5 SVs studied. A single RMS measurement was extracted from the \tilde{t}_r''' time history corresponding to the dominant signal of each FAI.

dominant signals with nominal RMS levels (2.5 ns or below) in the corresponding \tilde{t}_r''' traces. The resulting overlapping Allan deviation, shown in Fig. 11, reveals the average short-term stability of v1.0 and v1.5 frame clocks. Because frame slot occupancy is based on user demand, and therefore stochastic, the Allan deviation is derived from irregularly spaced data, as in [44]. But for every averaging time τ shown in Fig. 11, there were at least 1500 samples from which to estimate the corresponding Allan variance $\sigma_y^2(\tau)$, enough to yield highly accurate variance estimates.

Given the processing and data selection involved in creating the \tilde{t}_r''' time histories on which the composite Allan deviation plot shown in Fig. 11 is based, which tends only to remove variation, the plot should be taken as a lower bound on the frame clock stability of v1.0 and v1.5 Starlink SVs. This best-case stability is broadly consistent with a temperature-compensated crystal oscillator (TCXO). For example, at an averaging time of $\tau = 1$ s, the fractional frequency deviation is $\sigma_y(\tau) = 2.5 \times 10^{-9}$, which is what one would expect from an average-quality TCXO. Thus, we may conclude that the short-term stability of the Starlink v1.0 and v1.5 frame clocks is no better than that of a TCXO, though, as will be shown, it can episodically be much worse. One should bear

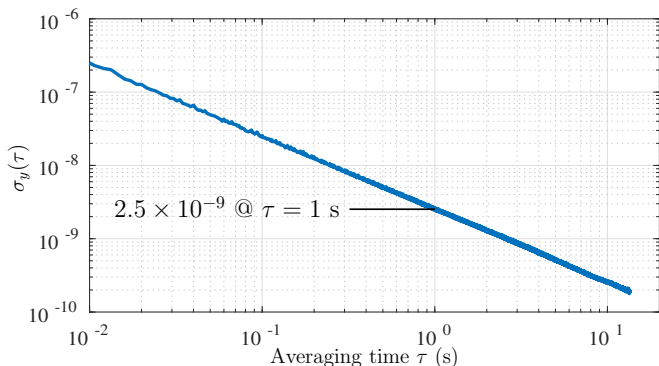


Fig. 11: Overlapping Allan deviation of a composite frame clock constructed from 18 \tilde{t}_r'' time histories originating from 9 distinct v1.0 and v1.5 Starlink SVs.

in mind, however, that a TCXO-quality base oscillator would not preclude highly accurate pseudorange-based PNT. It is true that all traditional GNSS SVs employ highly stable atomic oscillators [39], but a PNT service fused with a broadband LEO communications service could get by with much cheaper and less stable clocks by sending near-zero-age clock models to users through its high-capacity communications channels. For example, assuming the Allan deviation shown in Fig. 11, clock model updates at 1 Hz (corresponding to an averaging time of $\tau = 1$ s) would be sufficient to keep satellite clock modeling errors in the PNT solution below about 2.5 ns.

D. Anomalous Frame Clock Behavior

The foregoing jitter and stability results apply only for nominal behavior of the Starlink frame clock, which holds for approximately half of the FAIs studied. The other half manifest various modes of high-frequency frame clock instability. We do not know the underlying cause of these anomalous frame clock behavior modes, but we note here certain patterns of behavior and offer conjectures about their meaning.

Consider the top three panels of Fig. 10, which show the flattened time series \tilde{t}_r''' for 10-s intervals within three separate FAIs. The top panel shows nominal behavior, with 1.8 ns RMS, and acts as a baseline for comparison. The second panel shows much higher-RMS variations with significant time correlation. In this example trace, the deviations are bounded between -13 ns and 28 ns and include strong frequency components at 7.2 and 13.7 Hz. We classify anomalous frame clock behavior as oscillatory, as in this example, when one or two spectral components dominate. The third panel shows a \tilde{t}_r''' time history with sudden and irregularly spaced deviations, e.g., at the 2.6 s and 5.4 s marks. We classify such behavior as excursive.

The bottom panel of Fig. 10 shows a histogram of \tilde{t}_r''' RMS values for all v1.0 and v1.5 SVs studied. Each sample contributing to the histogram is a scalar RMS measurement extracted from the \tilde{t}_r''' time history corresponding to the dominant signal of a single FAI. Of the 48 FAIs studied,

- 22 exhibited nominal frame clock behavior, with RMS values below 2.5 ns;

- 19 exhibited oscillatory behavior, with RMS values above 2.5 ns and having a principal frequency component typically residing between 12 and 14 Hz;
- 3 exhibited excursive behavior;
- and 4 exhibited other behaviors, such as a mix of oscillatory and excursive modes, or elevated RMS values but without sudden excursions or dominant frequency components.

A clue to the origin of anomalous frame clock behavior may be found in the following remarkable observation: Whatever mode the frame clock manifests—whether nominal, oscillatory, excursive, or otherwise—invariably persists during a full FAI, but can switch to a different mode in the next FAI, even for the same SV. In fact, the traces in the top three panels of Fig. 10 are for the same Starlink SV during three contiguous FAIs. From this clue we conclude that anomalous behavior is connected to satellite hardware or software configuration changes that occur at FAI boundaries. For example, it may be that each of the three traces in Fig. 10 comes from an assigned beam cast by a different one of the serving Starlink SV’s downlink phase arrays, of which each SV has three. If the three phased arrays are driven by separate clocks, each with its own characteristic high-frequency behavior, this would explain the FAI-aligned frame clock mode switching. Alternatively, it may be that the baseband frame assembly process is governed by parameters set in software that remain fixed over each FAI, and that some parameter combinations lead to nominal frame clock behavior whereas others lead to anomalous modes.

One might suspect that apparent frame clock mode switching is actually unrelated to any clock but instead due to complications in the TOA measurement process. For example, oscillatory measurement errors might be caused by the interaction of assigned beams and side beams whose frame slots are closely aligned in composite signals. Relatedly, excursive measurement errors could be caused by the TOA measurement process occasionally misidentifying a side peak of the PSS + SSS autocorrelation function as the primary peak in low SNR conditions. Both of these possibilities have been investigated and discarded. In fact, anomalous frame clock modes can manifest even in simplex signals (no significant side beam peaks) with extremely high SNR. For example, an FAI captured from STARLINK-3894 (v1.5) showed a mix of oscillatory and excursive frame clock behavior with \tilde{t}_r''' RMS equal to 15 ns despite being an extraordinarily clean simplex signal with post-correlation SNR of 41 dB. Conversely, composite signals (one or more significant side beam signals), even with relatively low SNR, routinely yield \tilde{t}_r''' RMS below 2.5 ns. Clearly, the anomalous frame clock behavior is inherent in the frame clock deviation δt_f and not in any oddity of the TOA measurement process.

As with the 1-Hz clock adjustments, the anomalous frame clock variations discussed here would tend to degrade pseudorange-based PNT solutions formed from frame TOA measurements. While the root cause of anomalous frame clock behavior remains a mystery, we emphasize that nearly half of the FAIs studied showed nominal frame clock jitter, with RMS values below 2.5 ns. Clearly, the Starlink v1.0 and v1.5 baseband frame assembly process, and at least a large fraction

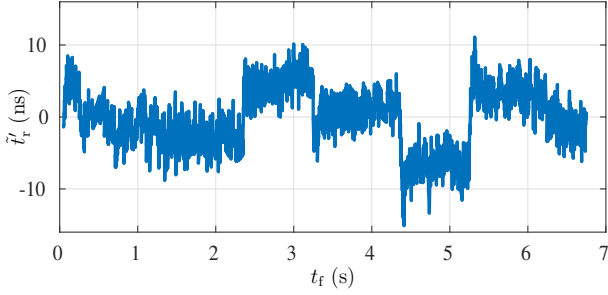


Fig. 12: As the top panel from Fig. 8 but for a v2.0-Mini SV. The data shown are for STARLINK-30178 from signals captured in February 2024.

of its base oscillators, have sufficient stability to support high-accuracy pseudorange-based PNT, provided the 1-Hz frame clock adjustments could somehow be modeled or eliminated.

E. Starlink v2.0 Frame Clock

We also generated \tilde{t}'_r time histories for v2.0-Mini SVs, an example of which is shown in Fig 12. These revealed frame clock adjustment behavior differing from that of v1.0 and v1.5 SVs in two ways: (1) the adjustments' magnitudes were generally much smaller, and (2) the adjustments occurred at irregular intervals, as opposed to the regular 1-Hz intervals for v1.0 and v1.5 SVs. Apparently, the Starlink v2.0-Mini SVs employ a different mechanism for base oscillator GNSS disciplining.

For v2.0-Mini SVs, the RMS values of the flattened time series \tilde{t}'''_r are higher than for the v1.0 and v1.5 SVs, ranging from 2.4 to 13.3 ns. There are three possible explanations for this: as compared to the v1.0 and v1.5 SVs, the v2.0-Mini SVs could have (1) oscillators with worse high-frequency stability, (2) a higher-noise GNSS disciplining technique, or (3) a frame clock that adds more high-frequency noise to the base oscillator signal t_d . Even still, the high-frequency jitter in the v2.0-Mini δt_f would not preclude meter-accurate pseudorange-based positioning because a batch of consecutive frame TOAs could be averaged to mitigate the higher jitter.

VIII. ABSOLUTE FRAME TIMING

Evidence of base clock GNSS disciplining raises the possibility that Starlink frames are continuously steered toward alignment with GPST. If true, this would be a notable discovery, inviting immediate use of Starlink for opportunistic pseudorange-based PNT. One could assume $\delta t_f(t) = 0$ for both assigned and side beams, which would be accurate to within the 1-Hz adjustment amplitude standard deviation, $\sigma_a = 117$ ns, or about 35 m in equivalent distance. Combining this satellite clock error model with publicly accessible Starlink ephemerides that are accurate (at least periodically) to within about $\sigma_e = 10$ m [45], one could form pseudoranges from a sequence of measured frame TOAs and process these with standard GNSS algorithms to obtain a position and time solution. Single-epoch 95% horizontal solution accuracy in this context can be approximated in meters as $\sqrt{4 \cdot \text{HDOP} (c^2 \sigma_a^2 + \sigma_e^2)}$

[15], where HDOP is the horizontal dilution of precision factor and c is the speed of light in vacuum. Given multiple signals from unique Starlink SVs with favorable geometry, HDOP could be as low as 0.55 [15], yielding a 95% horizontal error less than 54 m, tight enough for many applications of practical interest.

But if the frame clock is not transparent ($t_f \neq t_d$ in Fig. 3), then it may introduce errors that drive frame timing far from alignment with GPST despite the base clock being GNSS disciplined. This could render errors based on the simplistic clock model $\delta t_f(t) = 0$ too large for any useful PNT solution. A more sophisticated clock error model would be required.

This section addresses the question of whether Starlink frames are aligned with GPST. We first describe the methods used to deduce the time of transmission (TOT) in GPST of the m th frame of the l th FAI, written $t^*(l, m)$, given the corresponding frame TOA in GPST, $t_*(l, m)$. We then solve for $\delta t_f(l, m)$ and draw conclusions about Starlink frame clock steering and FAI alignment to GPST. For this initial study, it will suffice to determine $t^*(l, m)$ to better than $\sigma_a = 117$ ns.

A. Time of Transmission Calculation

TOT calculation begins with the frame TOA measurement $\tilde{t}_r(l, m)$ modeled in (20). We subtract from this an estimate of the offset $\delta t_{r,l,m}$ obtained from the simultaneously captured GNSS signals, accounting for all cable delays, as described in Section II. This process allows us to determine $t_*(l, m)$ to within a few ns, which, in turn, is related to $t^*(l, m)$ by

$$t^*(l, m) = t_*(l, m) - \delta t_{\text{tof}}(l, m) \quad (23)$$

What remains is to calculate the frame's time of flight, $\delta t_{\text{tof}}(l, m)$, modeled as

$$\delta t_{\text{tof}}(l, m) = \frac{1}{c} \cdot \|\mathbf{r}_r(t_*(l, m)) - \mathbf{r}_t(t^*(l, m))\| + \delta t_{\text{atm}} \quad (24)$$

where $\mathbf{r}_r(t_*(l, m))$ is the receiver's location at the TOA, $\mathbf{r}_t(t^*(l, m))$ is the transmitter's location at the TOT, and δt_{atm} is the atmospheric (neutral and ionospheric) delay experienced by the signal over its path from transmitter to receiver. Substituting (23) into (24) yields the implicit relationship

$$\delta t_{\text{tof}}(l, m) = \frac{1}{c} \cdot \|\mathbf{r}_r(t_*(l, m)) - \mathbf{r}_t(t_*(l, m) - \delta t_{\text{tof}}(l, m))\| + \delta t_{\text{atm}} \quad (25)$$

from which $\delta t_{\text{tof}}(l, m)$ can readily be calculated numerically, provided δt_{atm} and smooth transmitter and receiver location functions $\mathbf{r}_t(t)$ and $\mathbf{r}_r(t)$.

To support determination of $t^*(l, m)$ to within $\sigma_a = 117$ ns, errors in $\mathbf{r}_t(t)$, $\mathbf{r}_r(t)$, and δt_{atm} must be small relative to this amount. For δt_{atm} , a Saastamoinen [46] neutral atmospheric model with average surface parameters was applied with Niell wet and dry mapping functions [47]; ionospheric delays, which are minimal at Ku-band, were ignored. Errors in δt_{atm} for all elevation angles are expected to be less than 20 ns. The receiver location $\mathbf{r}_r(t)$ was approximated as constant, i.e., $\mathbf{r}_r(t) = \mathbf{r}_r$. Although the true location, the antenna feedhorn's phase center, moves by up to one meter as the dish assembly rotates to track SVs, omission of this movement

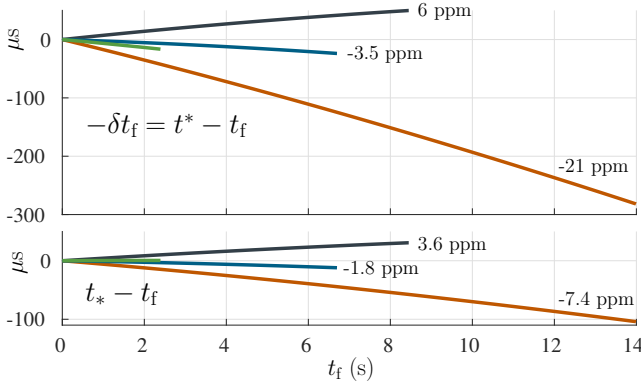


Fig. 13: Deviation of true frame TOT (top) and true frame TOA (bottom) from t_f for subintervals of four representative FAIs from three different Starlink v2.0-Mini SVs. For visual clarity, each trace has been shifted vertically to begin at an offset of zero. Colors indicate corresponding FAIs. Numerical labels indicate the clock drift in parts per million.

from $\delta t_{\text{tof}}(l, m)$ calculations introduces negligible timing error compared to σ_a .

Determination of $\mathbf{r}_t(t)$ required more careful treatment. While public providers of orbital data such as Celestrak and SpaceTrack offer regularly updated ephemerides for all operational Starlink SVs, neither source reliably publishes these data continuously at the required precision. Most open-access ephemeris providers, including Celestrak, publish data as two-line elements, which typically exhibit km-level uncertainty at epoch. This is insufficient: km-level position uncertainty corresponds to μs -level timing uncertainty. SpaceTrack ephemerides offer meter-level positioning for all Starlink SVs; however, such precision is only available for a short time after epoch, with $1\text{-}\sigma$ position uncertainty climbing to 10 meters in less than one hour. This would have sufficed if the data refresh epochs were predictable so that signal captures could be set to coincide with ephemeris epochs. But SpaceTrack refreshes Starlink ephemerides up to thrice a day with epochs that vary randomly by several hours. As such, use of SpaceTrack datasets for $\mathbf{r}_t(t)$ was deemed impractical for the purposes of this paper.

Instead, we developed our own ephemeris models based on raw observables produced by the onboard GNSS receivers of a small number of v2.0-Mini SVs. These observables, provided by SpaceX and processed through our GRID receiver’s central estimator as configured for LEO dynamics and a TCXO clock model, yielded discrete position solutions with formal errors below 10 m ($1\text{-}\sigma$). Position solutions were then fit over 12-13-min intervals with a 9th-order Chebyshev polynomial to yield a smooth $\mathbf{r}_t(t)$. Fit residuals were below 0.5 m RMS per dimension.

B. Clock Steering

We define clock steering as the process by which a clock is adjusted to match a reference time such that the clock offset does not drift significantly over relatively long (> 10 s) durations.

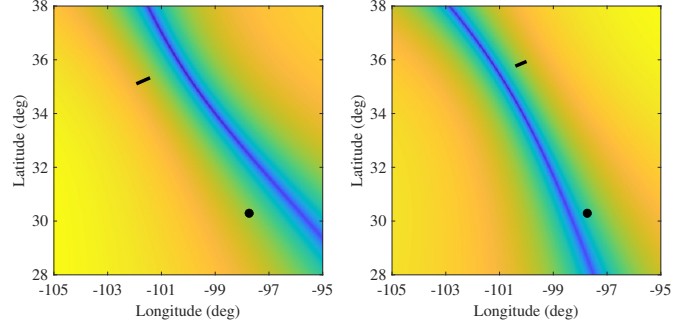


Fig. 14: Cost (on a dB scale) over the location search grid for ideal TOA clock steering. The left plot shows minimum-drift grid search results generated for the black line in the top panel of Fig. 13, whereas the right plot shows the same for the blue line. Both datasets originate from a capture taken from STARLINK-30178 in February 2024. Each plot’s black circle represents the true receiver location. The black line shows the satellite ground track over the trace’s time interval. Hot (yellow) areas signify areas experiencing degraded frame clock pre-compensation, while cold (blue) areas signify areas experiencing improved frame clock pre-compensation.

The top panel in Fig. 13 presents four frame clock deviation traces $-\delta t_f(l, m) = t^*(l, m) - t_f(l, m)$. These traces exhibit clock drift magnitudes varying from 0.2 to 21.4 ppm, values characteristic of a TCXO at best and a basic quartz oscillator at worst. The bottom panel shows frame clock deviations calculated from the same FAIs but substituting TOA in the place of TOT. We observe that all $t_* - t_f$ traces exhibit less deviation than their corresponding $t^* - t_f$ traces in the top plot. This suggests that Starlink SVs may be implementing frame clock pre-compensation to account for $\delta t_{\text{tof}}(l, m)$ changes as an SV passes overhead, thus mitigating the amount of frame clock drift experienced by Starlink receivers. Nonetheless, with long-term drift magnitudes ranging from 0.2 to 7.4 ppm, even the pre-compensated frame clock drift is far from ideal for pseudorange-based PNT.

It is worthwhile to consider the receiver location’s impact on the effectiveness of frame clock pre-compensation. Pre-compensation cannot apply perfectly for all receivers in a given service cell, since the evolution of $\delta t_{\text{tof}}(l, m)$ changes with \mathbf{r}_r . Possibly, a Starlink SV pre-compensates such that receivers at the center of a service cell experience ideal clock steering ($t_* - t_f = 0$). To explore this possibility, we conducted a least-squares location search on a grid spanning 10° each of latitude and longitude constrained to the surface of the WGS84 ellipsoid for two separate FAIs, those corresponding to the black and blue traces of Fig. 13. For each gridpoint, a trace was constructed as

$$t_*(l, m) - t_f(l, m) = t^*(l, m) + \delta t_{\text{tof}}(l, m) - t_f(l, m) \quad (26)$$

where $\delta t_{\text{tof}}(l, m)$ is the time of flight from the transmitter to the gridpoint’s location (rather than our receiver’s). The gridpoint was then assigned a corresponding squared sum cost $J = \sum_{m \in \mathcal{M}_l} [t_*(l, m) - t_f(l, m)]^2$, where \mathcal{M}_l represents all available occupied frame indices of the l th FAI. The results

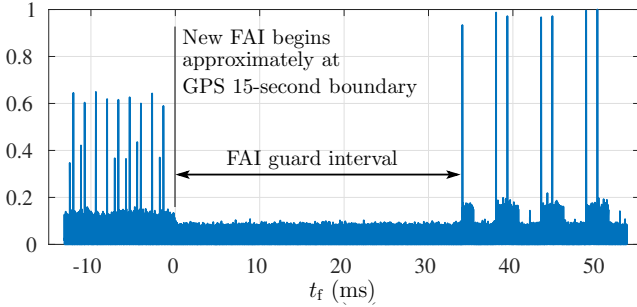


Fig. 15: Normalized cross-correlation of received Starlink data against a local PSS + SSS replica showing the boundary between subsequent FAIs.

are shown in Fig. 14. Examination of the minimum-drift valley indicates that even in the best cases, $t_*(l, m) - t_f(l, m)$ traces still exhibited 0.1 ppm of gross clock drift. While this is certainly an improvement, it remains difficult to predict where the minimum-drift location will be. Consider that the two minimum-drift search results are generated for the same SV but for different FAIs, yet the minimum-drift valleys are far apart and differ in shape. Moreover, they appear unconnected with the location of the service cell or the SV’s ground track. We conclude that Starlink frame timing is not driven towards alignment with GPST in a way that is both precise and predictable.

C. Fixed Assignment Interval Timing

The foregoing subsection showed that, during each FAI, Starlink frame timing is not driven toward alignment with GPST, whether at the SV or the target service cell. But it turns out that the frame clock does attempt approximate alignment with GPST at the beginning of each FAI. Fig. 15 shows the boundary between two successive FAIs; call these the $(l-1)$ th and l th FAIs. Note that frame occupancy in the visible segment of the $(l-1)$ th FAI appears maximal. Based on this, we assume that the final frame slot of the $(l-1)$ th FAI, whose index is $N_a - 1$, is occupied.

The l th FAI begins with the variable-length guard interval $T_{ag}(l) = N_{ag}(l)T_f$. Analysis of a dozen such boundaries revealed that $16 \leq N_{ag}(l) \leq 26$. We then calculated the true TOT for the final frame of the $(l-1)$ th FAI, denoted $t^*(l-1, N_a(l)-1)$, and estimated the true start time of the l th FAI as $t^*(l, 0) = t^*(l-1, N_a(l)-1) + T_f$. For the data shown in Fig. 15, $t^*(l, 0) = 514919.996874594$ when expressed in GPS seconds of week. Note that this is within about 3 ms of 514920, which is evenly divisible by 15. A similar pattern was evident in all such FAI transitions examined, from which we conclude that $t^*(l, 0)$ ranges between 4 and 2 ms before a 15-s GPST boundary. This finding may be expressed symbolically as

$$\lceil t^*(l, 0) \rceil - t^*(l, 0) \in [2, 4] \text{ ms} \quad (27)$$

$$\lceil t^*(l, 0) \rceil \bmod 15 = 0 \quad (28)$$

where $\lceil \cdot \rceil$ denotes the ceiling function and $l \in \mathbb{N}$.

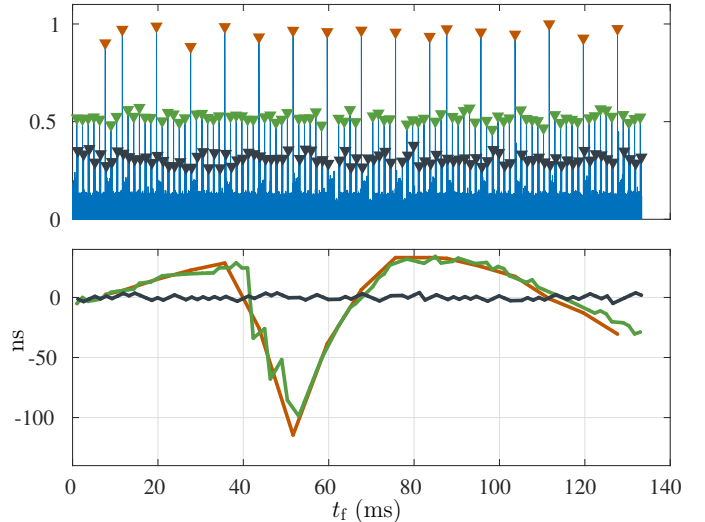


Fig. 16: Top: Normalized cross-correlation of received Starlink data against a local PSS + SSS replica over 100 frame intervals, showing peak trains from a dominant (probably assigned) beam (orange) and from two side beams (green and black). Bottom: Corresponding measured frame TOA time histories \tilde{t}_r with a linear trend removed from each. The data shown are for STARLINK-4577, a v1.5 SV, from signals captured in November 2023.

We also examined the true TOA $t_*(l, 0)$ and found that, while closer to an integer second, the range of variation was also approximately 2 ms, so it does not appear that FAI boundary timing is being steered into precise alignment with GPST at the location of the target service cell.

IX. COMPOSITE SIGNAL ANALYSIS

All frame timing results presented so far have been for dominant signals, typically from assigned beams. But deeper insight into the Starlink timing architecture can be gained by examining all constituent signals—both primary and secondary—of composite signals. One might be curious to know, for example, how closely secondary signals’ frames are aligned with those of primary signals, whether they experience the same 1-Hz adjustments and excursions, and whether primary and secondary signals manifest similar levels of jitter. The answers to such questions would indicate whether the clock cascade in Fig. 4 should be thought of as beam-specific, phased-array-specific, or otherwise.

The composite signal shown in the top panel of Fig. 16 is an informative example in this regard. It consists of a dominant signal, marked in orange, and two clear secondary signals, marked in green and black. In the interval shown, the dominant signal experiences a large (150-ns) excursion, evident in the orange trace of the lower panel. Notably, one of the secondary signals exhibits nearly the same excursion whereas the other does not. What is more, just 250 ms before the interval shown there occurred a 1-Hz adjustment of the type discussed in Section VII-A. Different from the excursion, this adjustment affected all three signals identically. All composite signals we studied followed the same pattern: excursions and oscillations

TABLE I: Signal Statistics for Fig. 16

Signal	Frames	SNR (dB)	Offset (ns)	RMS (ns)	$\beta_f \times 10^5$
Orange	17	28	0	37.2	-1.2 ± 0.0014
Green	80	23	4.3	31.2	-1.2 ± 0.0006
Black	95	20	2.6×10^5	1.8	-1.1 ± 0.0005

may differ among beams of the same SV, but adjustments do not. This pattern implies a clock cascade model in which a single base oscillator underlies all transmissions from a given SV, but separate frame clocks drive disjoint subsets of the SV’s beams.

For each signal in Fig. 16, Table I gives the number of frames whose TOAs were measured, the post-correlation SNR, the frame phase offset relative to the dominant signal’s phase, the RMS of the detrended traces in the bottom panel of Fig. 16, and the frame rate offset parameter β_f . The latter is a measure of how compressed or stretched the signal’s frame TOAs are compared to an exact $F_f = 750$ Hz cadence. The values for β_f are derived from a least-squares fit to the TOA time history for each signal. For the signals marked in orange and green, the excursion was removed before performing the least-squares fit. The uncertainty range shown for β_f is $\pm\sigma_f$, where σ_f^2 is the least-squares error variance for β_f assuming TOA measurement noise deviation $\sigma_w = 2$ ns.

The quantity β_f is the analog of the CFO parameter β but for the frame rate rather than the carrier frequency. For all traditional GNSS, $\beta_f = \beta$ for received signals (to within minor ionosphere-induced code-carrier divergence) because the same clock drives both carrier and spreading code generation. The local PSS + SSS replica in (18) also assumes identical β for both the carrier and the modulation $x_{m01}(t)$. But Table I identifies β_f as distinct from β because we discovered that $\beta_f = \beta$ does not hold universally for Starlink signals.

Table I indicates that the orange and green signals, which both experience the excursion, are also closely tied in other ways: their frame intervals are nearly perfectly aligned (within 4.3 ms), and they have identical β_f values. Contrarily, the excursion-free signal has a frame phase far from the other two (amounting to an offset of nearly 20% of the frame interval T_f) and a significantly different β_f value. For all three signals, the CFO parameter $\beta = (1.06 \pm 0.025) \times 10^{-5}$, where the uncertainty range comes from Fig. 6 for -10 dB pre-correlation SNR, a conservative bound for the signals in Fig. 16. Thus, in this case as in many others studied, β_f and β are significantly different—even different in sign. More generally, we found that $\beta_f = \beta$ only holds for about half of the FAIs studied, and that the condition $\beta_f = \beta$ can change at FAI boundaries for the same SV. This supports a clock cascade model in which $\Delta t_f(t)$ and $\Delta t_c(t)$ in (1) and (2) are independent.

X. CONCLUSIONS

Based on our study of Starlink v1.0, v1.5, and v2.0-Mini frame timing, we draw the following conclusions (C) and make the following conjectures (G) about Starlink’s timing architecture.

- C1 Beam-to-cell assignments remain static over 15-s fixed assignment intervals (FAIs). Each downlink beam carries a sequence of frames containing user data.
- C2 All beams cast by a given SV carry signals that are ultimately driven by the same base oscillator, but the signals may or may not share the same frame clock, which means that frame phase, rate, and short-term stability can differ significantly from beam to beam.
- C3 Periodic adjustments of the base oscillator cause large (~ 120 ns for v1.0 and v1.5 SVs, ~ 10 ns for v2.0-Mini SVs) abrupt deviations in frame timing that are common across all beams of the same SV.
- C4 Frame TOA jitter is nominally small (below 2.5 ns RMS), but frame timing can episodically manifest large unpredictable oscillations and excursions.
- C5 Frame TOA behavior can change on FAI boundaries, even for the same SV.
- C6 Frame short-term timing stability is ultimately limited by the quality of the base oscillator, which may be as good as, but no better than, a TCXO.
- C7 Frame timing is not driven toward alignment with GPST, whether at the SV or the target service cell. Rather, frames as transmitted can have a rate that is significantly different (e.g., 20 ppm) from the nominal $F_f = 750$ Hz rate.
- C8 FAIs are aligned within a few ms to a 15-s boundary of GPS seconds of week.
- C9 The carrier phase offset parameter β and frame rate offset parameter β_f may differ significantly, unlike with traditional GNSS signals, for which $\beta_f = \beta$ holds universally (to within minor ionosphere-induced code-carrier divergence).
- G1 The periodic adjustments seen in frame timing are the result of GNSS disciplining of the base oscillator.
- G2 The carrier signal is driven directly by the base oscillator, meaning that the carrier clock in Fig. 4 is transparent. By contrast, frames are assembled at baseband and then mixed to RF and modulated onto the carrier by a process that is subject to the variations (including those due to GNSS disciplining) of the base oscillator but that may impose additional frame timing and rate variations.
- G3 Signals having nearly identical frame rate offset parameter β_f and frame phase offset share the same frame clock.
- G4 Signals sharing the same frame clock are carried by beams emanating from the same downlink phased array, of which each Starlink SV has three.
- G5 Abnormal frame clock behaviors (oscillations, excursions) are not intentional. They are the result of frame packaging and modulation algorithms that satisfy communications requirements but take no special care to ensure frame timing stability.
- G6 The frame packaging and modulation algorithms are software-defined and could be updated to eliminate excursions and oscillations.

Three key implications (I) for pseudorange-based positioning and timing based on Starlink follow from the foregoing conclusions and conjectures:

- I1 Large and apparently unpredictable variations in frame timing, which can differ from beam to beam, and the lack of fine-grained frame phase steering toward a common time standard such as GPST, make Starlink currently unsuitable for purely opportunistic pseudorange-based PNT despite public availability of SV ephemerides.
- I2 Current Starlink SV hardware appears fundamentally capable of supporting pseudorange-based PNT with position and timing accuracy exceeding traditional GNSS.
- I3 There exist three options for making Starlink suitable for high-accuracy pseudorange-based PNT: (1) SpaceX could update Starlink’s software-defined frame clock to eliminate abnormal oscillations and excursions and to steer frames into precise (ns-level) alignment with GPST at the transmitter; (2) SpaceX could broadcast a low-latency frame clock model $\delta t_f(t)$ that would allow users to compensate for frame clock variations; (3) a third party could establish a network of reference stations that would measure Starlink frame TOA and send a low-latency frame clock model $\delta t_f(t)$ to its subscribers.

We note that option (2) could be limited to Starlink subscribers, whereas (1) and (3) would allow non-subscribers to benefit from Starlink-based PNT. A subscriber-limited version of (2) would involve bi-directional communication (at least for subscriber authentication), whereas a subscription-free version would enable passive (radio silent) Starlink-powered PNT. Option (3) would require a reference network dense enough to obtain accurate models $\delta t_f(t)$ for all unique frame clocks. In the worst case, this would require one reference receiver per ~ 20 -km-diameter service cell.

ACKNOWLEDGMENTS

Research was supported in part by the by the U.S. Department of Transportation under Grant 69A3552348327 for the CARMEN+ University Transportation Center, by Sandia National Laboratories, and by affiliates of the 6G@UT center within the Wireless Networking and Communications Group at The University of Texas at Austin. Sandia National Laboratories is a multi-mission laboratory managed and operated by National Technology & Engineering Solutions of Sandia, LLC, a wholly owned subsidiary of Honeywell International Inc., for the U.S. Department of Energy’s National Nuclear Security Administration under contract DE-NA0003525. This paper describes objective technical results and analysis. Any subjective views or opinions that might be expressed in the paper do not necessarily represent the views of the U.S. Department of Energy or the United States Government. The United States Government retains a non-exclusive, paid-up, irrevocable, world-wide license to publish or reproduce the published form of this article or allow others to do so, for United States Government purposes.

REFERENCES

[1] T. E. Humphreys, “Interference,” in *Springer Handbook of Global Navigation Satellite Systems*. Springer International Publishing, 2017, pp. 469–503.

[2] M. J. Murrian, L. Narula, P. A. Iannucci, S. Budzien, B. W. O’Hanlon, S. P. Powell, and T. E. Humphreys, “First results from three years of GNSS interference monitoring from low Earth orbit,” *NAVIGATION*, vol. 68, no. 4, pp. 673–685, 2021.

[3] Z. Clements, P. Ellis, and T. E. Humphreys, “Dual-satellite geolocation of terrestrial GNSS jammers from low Earth orbit,” in *Proceedings of the IEEE/ION PLANS Meeting*, Monterey, CA, 2023, pp. 458–469.

[4] G. S. Workgroup, “GPS spoofing: Final report of the GPS spoofing workgroup,” OPSGROUP, Tech. Rep., 2024. [Online]. Available: <https://ops.group/blog/gps-spoofing-final-report>

[5] W. Stock, R. T. Schwarz, C. A. Hofmann, and A. Knopp, “Survey on opportunistic PNT with signals from LEO communication satellites,” *IEEE Communications Surveys & Tutorials*, 2024.

[6] P. A. Iannucci and T. E. Humphreys, “Fused low-Earth-orbit GNSS,” *IEEE Transactions on Aerospace and Electronic Systems*, pp. 1–1, 2022.

[7] P. Gomez-del Hoyo and P. Samczynski, “Starlink-based passive radar for Earth’s surface imaging: first experimental results,” *IEEE Journal of Selected Topics in Applied Earth Observations and Remote Sensing*, 2024.

[8] Z. M. Kassas, N. Khairallah, and S. Kozhaya, “Ad astra: Simultaneous tracking and navigation with megaconstellation LEO satellites,” *IEEE Aerospace and Electronic Systems Magazine*, 2024.

[9] M. Neinaeva and Z. M. Kassas, “Cognitive sensing and navigation with unknown OFDM signals with application to terrestrial 5G and Starlink LEO satellites,” *IEEE Journal on Selected Areas in Communications*, 2023.

[10] N. Jardak and R. Adam, “Practical use of Starlink downlink tones for positioning,” *Sensors*, vol. 23, no. 6, p. 3234, 2023.

[11] C. Yang and A. Soloviev, “Starlink Doppler and Doppler rate estimation via coherent combining of multiple tones for opportunistic positioning,” in *2023 IEEE/ION Position, Location and Navigation Symposium (PLANS)*. IEEE, 2023, pp. 1143–1153.

[12] S. Kozhaya and Z. M. Kassas, “On the fundamental tracking performance and design considerations of radio navigation,” *IEEE Journal on Selected Areas in Communications*, 2024.

[13] M. L. Psiaki, “Navigation using carrier Doppler shift from a LEO constellation: TRANSIT on steroids,” *NAVIGATION*, vol. 68, no. 3, pp. 621–641, 2021.

[14] M. O. Moore, M. L. Psiaki, and R. M. Buehrer, “Time-diverse Doppler-only LEO PNT: Initial solution,” in *Proceedings of the ION GNSS+ Meeting*, 2024, pp. 3532–3541.

[15] P. A. Iannucci and T. E. Humphreys, “Economical fused LEO GNSS,” in *Proceedings of the IEEE/ION PLANS Meeting*, 2020.

[16] T. E. Humphreys, P. A. Iannucci, Z. M. Komodromos, and A. M. Graff, “Signal structure of the Starlink Ku-band downlink,” *IEEE Transactions on Aerospace and Electronic Systems*, pp. 1–16, 2023.

[17] Z. M. Komodromos, W. Qin, and T. E. Humphreys, “Weak signal acquisition and tracking of the Starlink Ku-Band downlink to enable global PNT,” in *Proceedings of the ION Joint Navigation Conference (JNC)*, 2024.

[18] S. Kozhaya, J. Saroufim, and Z. M. Kassas, “Starlink for PNT: A trick or a treat?” in *Proceedings of the 36th International Technical Meeting of the Satellite Division of The Institute of Navigation (ION GNSS+ 2023)*, 2024.

[19] W. Qin, Z. M. Komodromos, and T. E. Humphreys, “An agile, portable antenna system for LEO megaconstellation-based PNT,” in *Proceedings of the ION GNSS+ Meeting*, 2023.

[20] K. Wang and A. El-Mowafy, “LEO satellite clock analysis and prediction for positioning applications,” *Geo-spatial Information Science*, vol. 25, no. 1, pp. 14–33, 2022. [Online]. Available: <https://doi.org/10.1080/10095020.2021.1917310>

[21] H. Ge, T. Wu, and B. Li, “Characteristics analysis and prediction of low earth orbit (LEO) satellite clock corrections by using least-squares harmonic estimation,” *GPS Solutions*, vol. 27, no. 1, p. 38, 2023.

[22] C. Jiang, Z. Luo, M. Zhu, M. Guan, H. Zhu, and M. Gao, “Characteristics analysis of LEO satellite clock corrections and prediction by sliding estimation,” *Available at SSRN 4818891*, 2024.

[23] W. Qin, Z. M. Komodromos, and T. E. Humphreys, “An analysis of the short-term time stability of the Starlink Ku-band downlink frame clock,” in *Proceedings of the IEEE International Conference on Wireless for Space and Extreme Environments (WISEE 2024)*, 2024.

[24] H. A. Nichols, M. J. Murrian, and T. E. Humphreys, “Software-defined GNSS is ready for launch,” in *Proceedings of the ION GNSS+ Meeting*, Denver, CO, 2022.

[25] Z. Clements, P. A. Iannucci, T. E. Humphreys, and T. Pany, “Optimized bit-packing for bit-wise software-defined GNSS radio,” in *Proceedings of the ION GNSS+ Meeting*, St. Louis, MO, 2021, pp. 3749–3771.

- [26] T. Pany, D. Akos, J. Arribas, M. Z. H. Bhuiyan, P. Closas, F. Dovis, I. Fernandez-Hernandez, C. Fernández-Prades, S. Gunawardena, T. Humphreys, Z. M. Kassas, J. A. L. Salcedo, M. Nicola, M. L. Psiaki, A. Rügamer, Y.-J. Song, and J.-H. Won, "GNSS software defined radio: History, current developments, and standardization efforts," *NAVIGATION*, vol. 71, no. 1, 2024.
- [27] S. Pekhterev, "The bandwidth of the Starlink constellation and the assessment of its potential subscriber base in the USA," *SatMagazine*, vol. 11, pp. 54–57, 2021.
- [28] G. Huston, "A transport protocol's view of Starlink," May 2024, accessed: 2024-11-22. [Online]. Available: <https://blog.apnic.net/2024/05/17/a-transport-protocols-view-of-starlink/>
- [29] N. Mohan, A. E. Ferguson, H. Cech, R. Bose, P. R. Renatin, M. K. Marina, and J. Ott, "A multifaceted look at Starlink performance," in *Proceedings of the ACM on Web Conference 2024*, 2024, pp. 2723–2734.
- [30] E. Grayver, R. Nelson, E. McDonald, E. Sorensen, and S. Romano, "Position and navigation using Starlink," in *2024 IEEE Aerospace Conference*. IEEE, 2024, pp. 1–12.
- [31] Z. M. Komodromos, W. Qin, and T. E. Humphreys, "Signal simulator for Starlink Ku-Band downlink," in *Proceedings of the ION GNSS+ Meeting*, 2023, pp. 2798–2812.
- [32] A. Hills, J. M. Peha, J. Munk, and S. Pogorelc, "Controlling antenna sidelobe radiation to mitigate Ku-band LEO-to-GEO satellite interference," *IEEE Access*, vol. 11, pp. 71 154–71 163, 2023.
- [33] A. Hills, J. M. Peha, and J. Munk, "Feasibility of using beam steering to mitigate Ku-band LEO-to-GEO interference," *IEEE Access*, vol. 10, pp. 74 023–74 032, 2022.
- [34] J. Brodtkin. (2024, October) SpaceX claims Starlink can offer gigabit speeds if FCC approves new plan. [Online]. Available: <https://arstechnica.com/tech-policy/2024/10/spacex-claims-starlink-can-offer-gigabit-speeds-if-fcc-approves-new-plan/>
- [35] D. Odijk, "Positioning model," in *Springer Handbook of Global Navigation Satellite Systems*. Springer International Publishing, 2017, pp. 605–638.
- [36] O. Montenbruck, A. Hauschild, and P. Steigenberger, "Differential code bias estimation using multi-GNSS observations and global ionosphere maps," *NAVIGATION*, vol. 61, no. 3, pp. 191–201, 2014.
- [37] M. Meurer and F. Antreich, "Signals and modulation," in *Springer Handbook of Global Navigation Satellite Systems*. Springer International Publishing, 2017, pp. 91–119.
- [38] C. Jekeli and O. Montenbruck, "Time and reference systems," in *Springer Handbook of Global Navigation Satellite Systems*. Springer International Publishing, 2017, pp. 25–58.
- [39] R. Beard and K. Senior, "Clocks," in *Springer Handbook of Global Navigation Satellite Systems*. Springer International Publishing, 2017, pp. 121–164.
- [40] M. Skolnik, *Introduction to radar systems 2nd Edition*. McGraw-Hill, 1980.
- [41] D. Odijk and L. Wanninger, "Differential positioning," in *Springer Handbook of Global Navigation Satellite Systems*. Springer International Publishing, 2017, pp. 753–780.
- [42] P. Royston, "Approximating the Shapiro-Wilk W-test for non-normality," *Statistics and computing*, vol. 2, pp. 117–119, 1992.
- [43] R. M. Gray and D. L. Neuhoff, "Quantization," *IEEE Transactions on Information Theory*, vol. 44, no. 6, pp. 2325–2383, 1998.
- [44] C. Hackman and T. E. Parker, "Noise analysis of unevenly spaced time series data," *Metrologia*, vol. 33, no. 5, p. 457, 1996.
- [45] A. Liu, X. Xu, Y. Xiong, and S. Yu, "Maneuver strategies of Starlink satellite based on SpaceX-released ephemeris," *Advances in Space Research*, 2024.
- [46] J. Saastamoinen, "Atmospheric correction for the troposphere and stratosphere in radio ranging of satellites," in *Geophysical Monograph 15*, S. W. Henriksen, Ed. Washington, D.C.: American Geophysical Union, 1972, pp. 247–251.
- [47] A. E. Niell, "Global mapping functions for the atmosphere delay at radio wavelengths," *Journal of Geophysical Research*, vol. 101, pp. 3227–3246, 1996.